Available online at www.sciencedirect.com
ScienceDirect
Tectonophysics 466 (2009) 307–321
TECTONOPHYSICS
www.elsevier.com/locate/tecto

Subsurface structure, physical properties, fault-zone characteristics and stress state in scientific drill holes of Taiwan Chelungpu Fault Drilling Project

Jih-Hao Hung [a,*], Kuo-Fong Ma [a], Chien-Yin Wang [a], Hisao Ito [b], Weiren Lin [c], En-Chao Yeh [c,1]

[a] Institute of Geophysics, National Central University, Jhongli, Taiwan
[b] Center for Deep Earth Exploration, Japan Agency for Marine-Earth Science and Technology, Japan
[c] Kochi Institute for Core Sample Research, Japan Agency for Marine-Earth Science and Technology, Japan

Available online 22 November 2007

Abstract

Continuous cores and a suit of geophysical measurements were collected in two scientific drill holes to understand physical mechanisms involved in the large displacements during the 1999 Chi-Chi earthquake. Physical properties obtained from wire-line logs including P- and S-wave sonic velocity, gamma ray, electrical resistivity, density and temperature, are primarily dependent on parameters such as lithology, depth and fault zones. The average dip of bedding, identified from both cores and FMI (or FMS) logs, is about 30° towards SE. Nevertheless, local azimuthal variations and increasing or decreasing bedding dips appear across fault zones. A prominent increase of structural dip to 60°–80° below 1856 m could be due to deformation associated with propagation of the Sanyi fault.

A total of 12 fault zones identified in hole-A are located in the Plio-Pleistocene Cholan Formation, Pliocene Chinshui Shale and Miocene Kueichulin Formation. The shallowest fault zone occurs at 1111 m depth (FZ1111). It is a 1 m gouge zone including 12 cm of thick indurate black material. We interpreted this zone as the slip zone during Chi-Chi earthquake. FZ1111 is characterized by: 1) bedding-parallel thrust fault with 30-degree dip; 2) the lowest resistivity; 3) low density, V_p and V_s, 4) high V_p/V_s ratio and Poisson's ratio; 5) low energy and velocity anisotropy, and low permeability within the homogeneous 1 m gouge zone; 6) increasing gas (CO_2 and CH_4) emissions, and 7) appearance of smectite within the primary slip zone.

In situ stresses at the drill site were inferred from leak-off tests, borehole breakouts and drilling-induced tensile fractures from borehole FMS/FMI logs, and shear seismic wave anisotropy from DSI logs. The dominant fast shear-wave polarization direction is in good agreement with regional maximum horizontal stress axis, particularly within the strongly anisotropic Kueichulin Formation. A conjugate set of secondary directions are parallel to microcrack orientations. A drastic change of orientation of fast shear-wave polarization across the Sanyi thrust fault at the depth of 1712 m reflects the change of stratigraphy, physical properties and structural geometry.

Keywords: Chi-Chi earthquake; Taiwan Chelungpu Fault Drilling Project; Fault-zone properties; Borehole breakouts; S-wave anisotropy

1. Introduction

The 1999 Chi-Chi earthquake (M_w 7.6) produced over 90 km-long surface rupture zone along the north–south trending, west-vergent Chelungpu fault (MOEACGS, 2000; Fig. 1). The most striking feature of the coseismic displacement field in the hanging-wall is that areas of large surface displacement lie above the footwall ramp of the thrust and at the northern termination; by contrast, relatively smaller, but significant (1–3 m) displacements are recorded at the footwall detachment (Yu et al., 2001; Dominguez et al., 2003; Lee et al., 2003). Along strike, both horizontal and vertical components of surface displacements increase from south to north and reach up to 12 m at the northern end near the Shihgang area. Surface ruptures indicate that the Chelungpu thrust runs parallel in map-view to the hanging-wall of the Pliocene Chinshui Shale, which indicates that the fault plane is a detachment in the Chinshui Shale.

In map-view (CPC, 1982), south of Wufeng village, the Chelungpu fault merged with the Sanyi fault to the west into

* Corresponding author. 300 Jungda Road, Jhongli City, Taoyuan, 32001, Taiwan.
E-mail address: jhhung@ncu.edu.tw (J.-H. Hung).
[1] Now at the Department of Geological Sciences, National Taiwan University, Taipei, Taiwan.

0040-1951/$ - see front matter © 2007 Elsevier B.V. All rights reserved.
doi:10.1016/j.tecto.2007.11.014

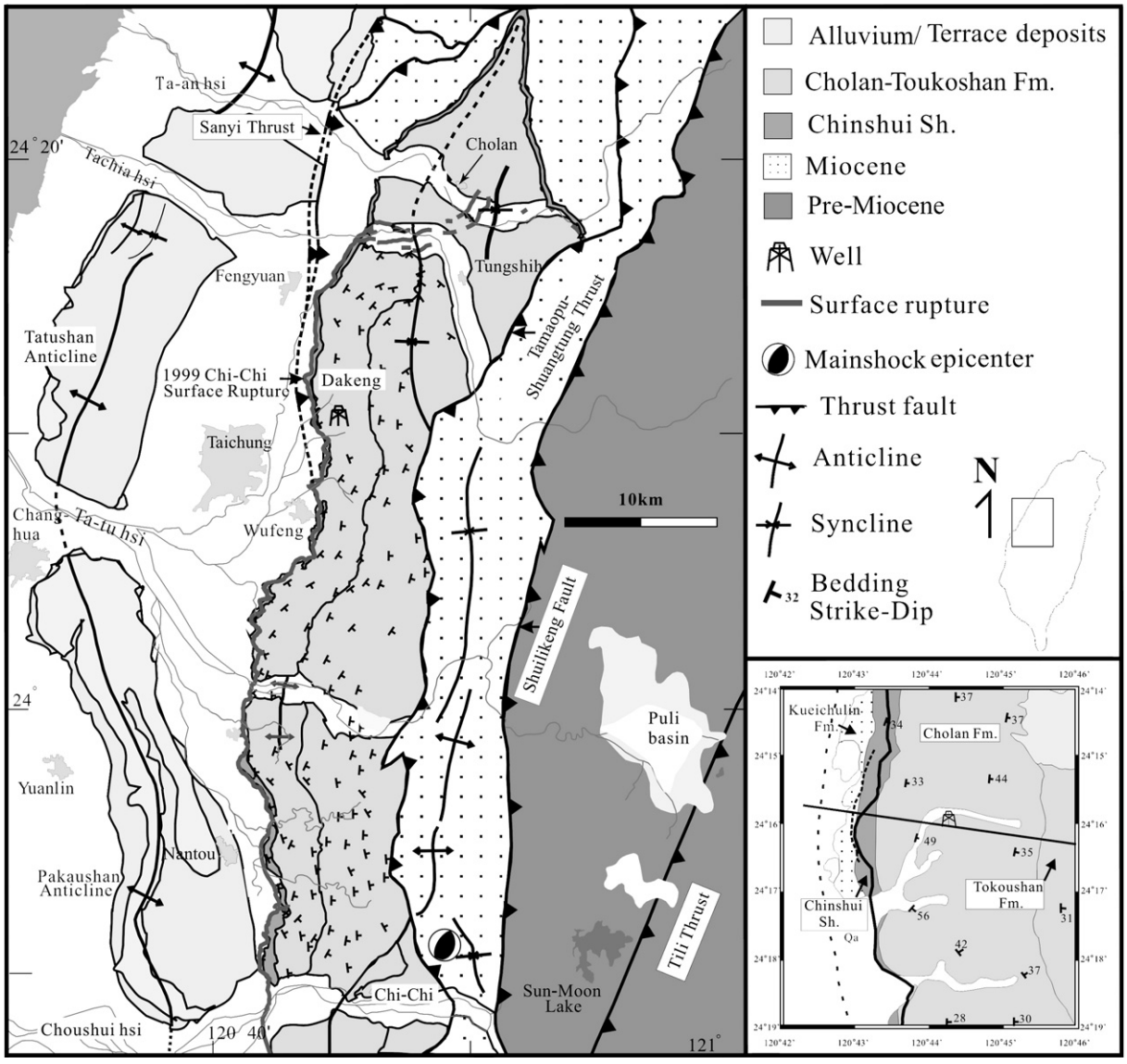

Fig. 1. Geologic map of the Chelungpu-fault area with location of the epicenter of the 1999 Chi-Chi main shock, surface ruptures (from MOEACGS, 2000) and the Dakeng drill site. Inset shows the stratigraphy near the drill site and location of structural section. Note that the rupture traces (thick lines) are confined within, but cut up and down within the Chinshui shale. Map modified from CPC (1982).

single fault (Chang, 1971; called Chelungpu-Sanyi fault hereafter) and emplaced the Pliocene Chinshui Shale on top of the Pleistocene Tokoushan Formation and Holocene deposits. The subsurface Chelungpu–Sanyi fault plane, imaged by both shallow and deep seismic profiling (Wang et al., 2002, 2004), shows a ramp-flat geometry from the base of the Chinshui Shale (Hung and Suppe, 2002; Yue et al., 2005).

Towards north, the Chelungpu–Sanyi fault branches into two segments (Fig. 1): a) the underlying fault, called Sanyi thrust, which steps up from a deeper Pliocene and late-Miocene detachment in the Kueichulin and Tungkeng Formations and is probably not active, and b) the North Chelungpu detachment (called Chelungpu fault hereafter) which is a relatively young, nearly bedding-parallel fault in the Chinshui Shale and is the focus of some largest displacements in the Chi-Chi earthquake. Subsurface investigations of northern fault segments through a number of shallow seismic (Wang et al., 2002), deep petroleum seismic profiles (Hung and Wiltschko, 1993) and shallow drilling (Tanaka et al., 2002; Huang et al., 2002) confirm that the near-surface segment of the Chelungpu thrust is parallel to both bedding and the underlying Sanyi fault to a depth of 3 km. The TCDP deep boreholes are drilled through this high-slip portion of the Chelungpu fault and through the Sanyi ramp in the footwall.

An important question that needs to be addressed is what physical properties or dynamic processes within the fault zone cause large coseismic displacement in the northern segment. Hypotheses have been proposed include: 1) change of the fault-plane geometry; 2) static (long-term) physical properties such as intrinsic low coefficient of friction, high pore-pressure and solution-transport chemical processes, and 3) dynamic change of physical properties during slip. A detailed three-dimensional

subsurface structure of the Chelungpu fault shows that surface coseismic displacements mimic the growth of active structures and geomorphology (Hung and Suppe, 2002). Areas of large displacements in the north of the Chelungpu fault could be associated with a reduction of overburden as a result of elevated Chelungpu ramp and flat (Yue et al., 2005).

The level of dynamic friction and stress during earthquake rupture is a key unknown, and are earthquake faults "low" or "high" strength? (Zoback et al., 1987; Hickman, 1991). If the coefficient of friction, μ, follows Byerlee's Law and ranges from 0.6 to 0.9 (Byerlee, 1978), frictionally generated heat should be observed near the Chelungpu fault zone (Mori et al., 2002). On the other hand, the presence of clay-rich fault gouges (Vrolijk and Van der Pluijm, 1999) and/or permanently high pore pressure (Hubbert and Rubey, 1959; Suppe and Wittke, 1977) within the fault zone can effectively reduce fault strength and the coefficient of friction. Other solution-transport mechanisms such as pressure solution, fluid-assisted mineral reactions may be important to determine the rheology of fault zones and the time scale of interseismic strength recovery (Blanpied et al., 1998; Rutter et al., 2001). The role of these mechanisms in determining the fault strength and earthquake instability mechanisms are unknown because of uncertainties regarding the mineralogy, microstructures and physical properties of fault-zone materials and nature and distribution of fluids at focal depths. Moreover, the "smooth" (low-level of high-frequency radiation) and "rapid" (high velocity) motion and large displacement in the north as opposed to larger accelerations and smaller displacements in the southern segment (Ma et al., 2000) may be attributable to the heterogeneity of fault rocks. The fault plane lies at contact of shale and conglomerate in the south but within the Chinshui shale in the region of large displacements as revealed by cores from two shallow holes drilled into the Chelungpu fault in the area near Nantou and Fengyuan, respectively (Huang et al., 2002). In this regard, the physical properties of the fault-zone material and width and roughness of the fault zone probably vary considerably along the fault, and this heterogeneity may play an important role for the above mechanisms to operate during the rupture propagation (Tanaka et al., 2002; Heermance et al., 2003).

Contrary to high rock strength from both laboratory experiments and in-situ stress measurement, many dynamic weakening mechanisms (Mori et al., 2002) include slip weakening (Scholz, 1998; 2002), thermal pressurization (Noda and Shimamoto, 2004; Wibberley and Shimamoto, 2005), mechanical lubrication (Ma et al., 2003) and melting (Hirono et al., 2006). To differentiate these broad ranges of mechanisms will require the knowledge of physical properties of fault rocks, heat flow and stress measurements before and after the earthquake to quantify the energy release in seismogenic zones (Wang, 2006). For example, physical examination of fault-zone rocks could make it possible to infer deformation mechanisms of fault zone and dynamic frictional characteristics.

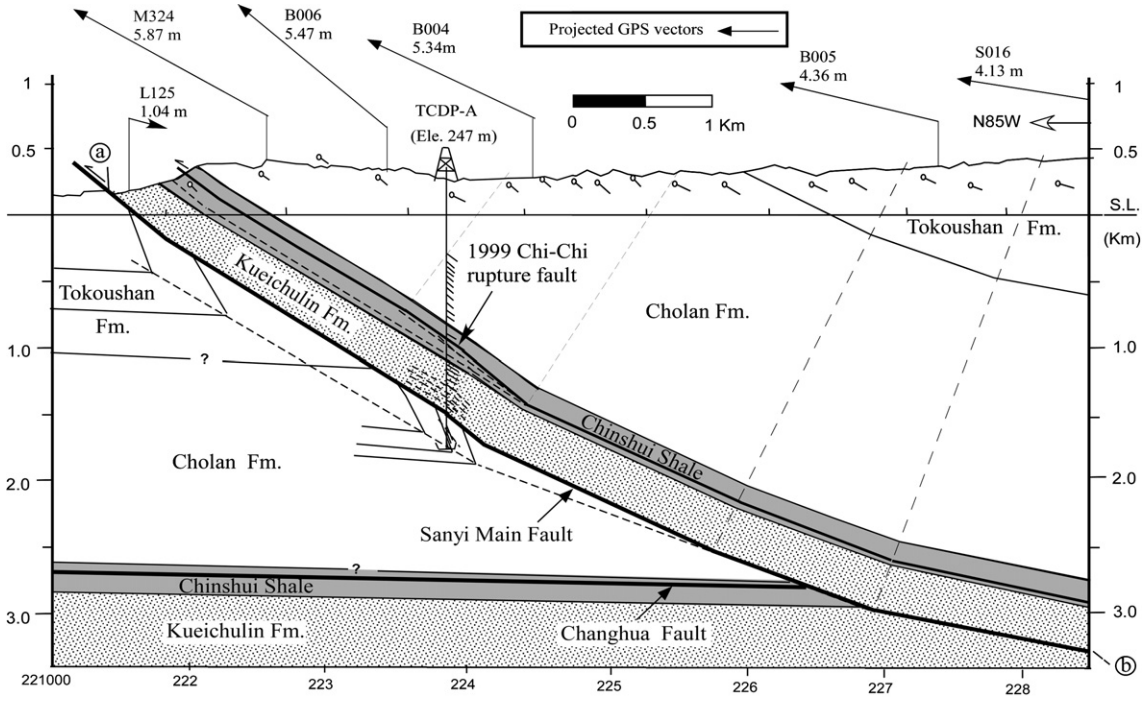

Fig. 2. Interpreted structural profile across the Dakeng well (hole-A) based on the surface and subsurface drilled data. Measured depth (from rig floor, 3 m above the ground level) intervals and true thickness (in parenthesis) of formations in this borehole includes: Cholan, 0–1013 m (877 m); Chinshui, 1013–1300 m (249 m), and Kueichulin 1300–1710 m (355 m). Underlying the Sanyi fault is the repeated section of Cholan formation from 1710–2003 m. Locations of Chelungpu (Chi-Chi rupture), Sanyi and interpreted Changhua faults are shown by solid lines. Older faults formed prior to the Chi-Chi earthquake are shown by dashed lines. The displacement of the Sanyi fault is greater than 9 km (from eroded base of hanging-wall cutoff point "a" to footwall cutoff point "b"). The GPS vectors are projected components of the coseismic displacement in the plane of section (station number and displacement are given; Yang et al., 2000). Note that the displacement vectors, except in the footwall of the rupture fault, are approximately parallel to the fault at depth.

To address the above questions two holes (A and B) were drilled for Taiwan Chelungpu Fault Drilling Project (TCDP) during 2004–2005 at Dakeng, west-central Taiwan, where large surface slip (~10 m, station M324 shown in Fig. 2) was observed. Continuously coring and geophysical down-hole logging in two holes 40 m apart were completed from a depth of 500 to 2003 m (hole-A) and 950 to 1350 m (hole-B). Down-hole long-term monitoring such as temperature and seismicity were deployed after the drilling. In this paper we integrate results from cores and wire-line down-hole geophysical logs to characterize subsurface structure, physical properties of formations and fault zones, focusing on the Chi-Chi rupture zone. In-situ stress measurements, high-resolution microresistivity images (FMI and FMS, both marks of Schlumberger) of the borehole wall and shear-wave velocity anisotropy provide stress state post-Chi-Chi earthquake around the drill site.

2. Geology at drill site and fault-zone characteristics

Surface geology (CPC, 1982) near the drill site shows that surface ruptures of the Chi-Chi earthquake are confined within but cuts up and down horizons of the Chinshui Shale (Fig. 1). Formations encountered in hole-A are mainly composed of clastic sedimentary rocks from Upper Miocene Kueichulin Formation to Pliocene Cholan formation. Precise locations of formation boundaries were made by, 1) correlating wire-line logs among hole-A and other nearby petroleum wells and 2) comparing stratigraphic sequence between surface outcrops and cores (Lin et al., 2007; Fig. 2). Reworked Miocene nannofossils

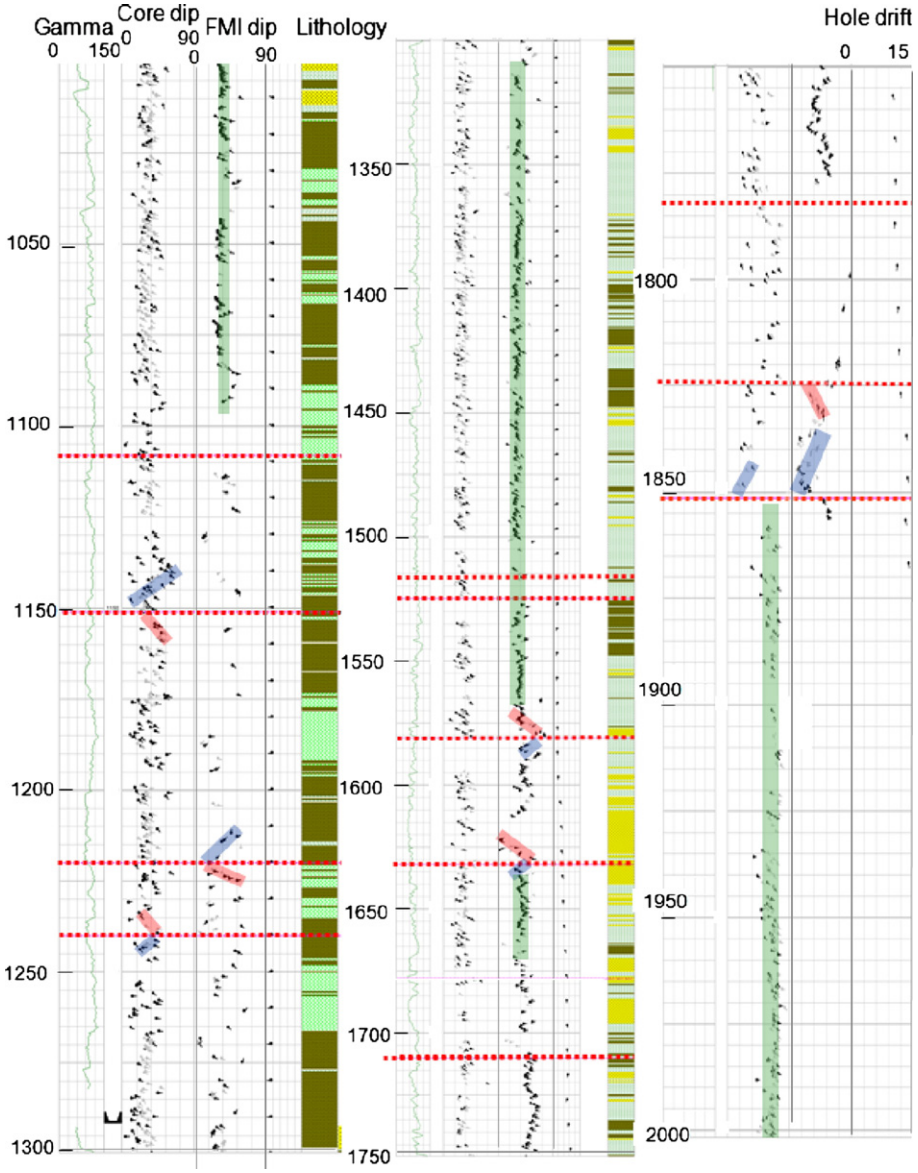

Fig. 3. Geometric relationship between fault zones and changes of bedding orientation derived from core (second track) and FMI images (third track). The casing shoe is located at 1300 m, and borehole drift is in last track. The dip pattern across faults is shown by changes in dip magnitude (increase, "red pattern" and decrease, "blue pattern") and dip azimuth (rotation or nonrotation) with depth, whereas strata exhibiting uniform orientation over a certain range are represented by green pattern.

Table 1
Locations (drilled depth) of fault zones and width of gouge and breccia (both total and hanging-wall inside parenthesis are given) in each fault zone identified from cores

Fault zone	Core depth (m)	Gouge/breccia (m)
FZ1111	1109.02–1111.83	1.12/1.68 (1.25)
FZ1153	1151.30–1153.92	0.50/2.12 (1.60)
FZ1222	1220.50–1221.93	0.25/1.18 (0.10)
FZ1241	1240.87–1241.86	0.10 (distribute thin gouge layers)
FZ1519	1518.80–1519.30	0.10/0.40 (0.40)
FZ1525	1524.07–1527.64	0.17/3.38 (1.38)
FZ1581	1581.20–1582.10	0.02/0.20 (0.10) (distributed gouge layers)
FZ1632	1632.45–1633.00	0.04/0.40 (distributed gouge layers)
FZ1712	1711.80–1713.15	1.00/0.35 (Nil)
FZ1785	1785.35–1785.65	0.30/Nil (Nil)
FZ1825	1824.57–1825.22	0.20/0.45 (0.25)
FZ1855	1855.09–1856.29	0.60/0.60 (0.50)

FZ1111 to FZ1241 are distributed within the Chinshui Shale and categorized as Chelungpu fault system, below which the rest fault zones are located in the Kueichulin and underlying Cholan formations and associated with Sanyi thrust system.
Note: 1. "Width" and "thickness" is distinguished by: "width" represents the core (drilling) length and "thickness" corresponds to the normal distance of a certain planer structure/layer.
2. Gouges with thickness more than 5 mm thick are counted in total thickness. Distributed thin gouge layers within breccia or protolith are not counted in.
3. FZ1222 is composed of cohesive, indurate fault rocks and is classified as "cataclasite".

and similar lithology to surface exposed Cholan Formation indicates that the footwall of the Sanyi fault is made up of repeated Cholan Formation.

The main Chelungpu–Sanyi fault has accumulated a displacement of about 14 km along the main ramp and detachment at the location of the main shock of the Chi-Chi earthquake (Yue et al., 2005). In the profile across the TCDP boreholes, the Sanyi thrust and Chelungpu fault are parallel faults, and slip occurs mainly on the underlying Sanyi fault. The geological displacement along the Sanyi thrust is at least 9 km (Fig. 2). A similar amount of slip was also found in the cross section along the Ta-an hsi to the north (Hung and Wiltschko, 1993). The total displacement on the Chelungpu fault is estimated about 0.3 km determined from coseismic uplifted Hsinhse terraces immediately north of the drill site (Hung and Suppe, 2002; Yue et al., 2005), The Chelungpu fault model is constrained by surface dips, subsurface borehole imaging and core observation. The projected GPS vectors show that the motion of the Chelungpu hanging-wall is proximately parallel to both bedding and the fault, which indicates that surface coseismic displacement is dominated by structural growth.

Regional bed attitude above FZ1712, identified from cores and FMI/FMS images in hole-A and from correlation of fault zones between hole-A and hole-B, is trending N15°–21°E, dipping 20°–40° (30° on average) toward SE (Fig. 3). Nonetheless, intervals of increasing (from 30° to 75°) or decreasing (from 70° to 20°) dip as well as changes of dip azimuth appear across fault zones (Fig. 3). A gradual increase of bedding dip with depth starts from FZ1712, and a drastic change of dip from 20°–40° to 60°–80° occurs across FZ1855 where steep to overturned beds extend to the bottom hole.

Table 2
Physical and structural features of fault zones from core and logging data (see text for explanation)

Fault zone	Gouge thickness (cm)	Color	Fluid content	Fault type	Lithology	Fault dip	Bed dip pattern
FZA1111	112	LG	High	Thrust 105/30	Silt/silt with Ss interbed	30	No drag No rotation
FZA1153	50	G	Low	Thrust 105/40	Silt with Ss interbed	40	Drag, no rotation Blue in HW Red in FW
FZA1222	25	G	Low	Thrust 015/28	Ss/silt	28	No drag Rotation
FZA1241	<5	BL	Dry	Normal 195/30	Silt/silt	30	Drag, no rotation Red in HW Blue in FW
FZA1519	10	G	Medium	N/A	Silt/Ss	30	No drag No rotation
FZA1525	15	G	Medium	Strike-slip 195/75	Ss/Ss	30	No drag Rotation
FZA1581	<0.5	G	High	Thrust 015/60	Mass Ss/Ss	30	Drag, rotation Red in HW Blue in FW
FZA1632	<0.5	G	Medium	N/A	Ss with interbed silt	30	Drag, Rotation Red in HW Blue in FW
FZA1712	100	G-DG	Medium	Thrust 105/30	Bioturbated Ss/layered Ss	30	No drag No rotation
FZA1785	30	DG	Low	N/A	Ss w/ interbed sandy Silt	20	Drag, no rotation Red in HW Blue in FW
FZA1825	20	DG	Low	N/A	Ss w/ interbed silt	20	Drag, rotation Red in HW Blue in FW
FZA1855	60	G	Medium	N/A	Silt/silt	60	Drag, rotation Blue in HW Red in FW

A total of 12 fault zones were identified in hole-A exclusive of zones of widely spaced, single shear fractures. The location, thickness, and physical and structural features of each fault zone are listed in Tables 1 and 2. The shallow 4 fault zones are located in the Chinshui Shale. FZ1241 is a normal fault; the rest three thrust faults can be categorized as part of the Chelungpu fault system. The detailed architecture of the above fault zones was discussed in Sone et al. (2007).The below 5 zones within the Kueichulin Formation can be grouped as the Sanyi fault system. The main Sanyi thrust is encountered at 1712 m, where the Kueichulin Formation overlies the Cholan Formation.

Common fault rocks in the cores include intensely deformed fault core (clayey gouge) and adjacent highly fractured damage zones (fault breccia). The fault gouge is composed of ultra-fine grained clay minerals and massive to foliated fabrics; occasionally thin layers of indurate black material appear within the gouge zone. The paucity of veins inside the fault zones indicate that these fault rocks are formed in low temperature and by fracturing process. Both microscopic observations of thin sections and XRD analyses show that major mineral compositions are similar in both fault and host rocks (Isaacs et al., 2007). A typical example is the Chelungpu fault zone, FZ1111. The fault is bedding-parallel consisting of fault breccia and fault gouge 1109 to 1112 m (Fig. 4). The degree of fracturing increases from the top of the damage zone towards the gouge zone in which the fabrics changed from massive to foliate between 1110.25 and 1111.35 m. The Chi-Chi major slip zone (MSZ, about 2 cm thick) is contained within the 12 cm thick primary slip zone (PSZ), which is located near the bottom of this broad gouge zone (Ma et al., 2006; Sone et al., 2007). FZ1712 is a major Sanyi fault zone that also contains about 1 m of clayey gouge and a thrust-fault type with nearly consistent bedding attitude in both the hanging- and footwalls (see Fig. 3).

The thickness of each fault zone can range from tens of centimeters to a few meters (Table 1) and the spatial distribution of gouge and breccia can be heterogeneous. For example, the thickness or distribution of breccia is not symmetrical around

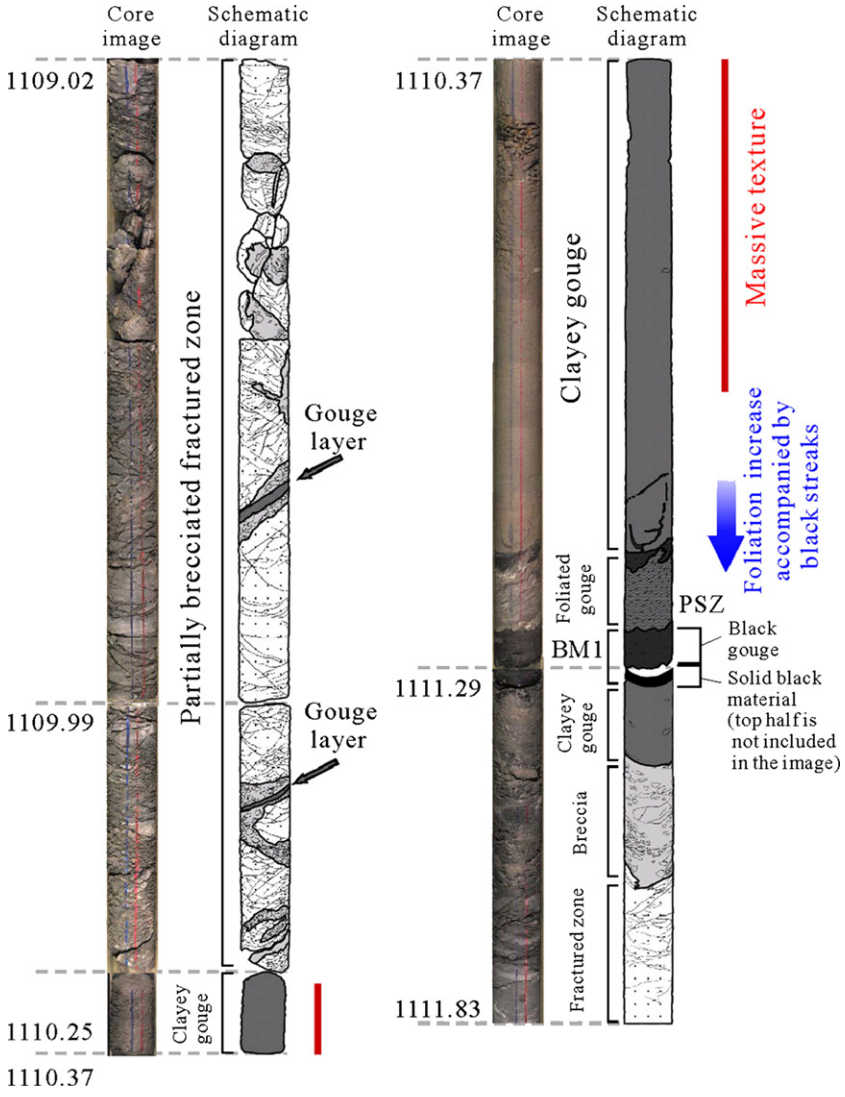

Fig. 4. The core image and sketch diagram of fault zone FZ1111 from depth 1109.02 m to 1111.83 m of hole-A with descriptive comments. Note the degree of deformation increases to the bottom of clayey gouge zone and a 12-cm primary slip zone develops at depth of 1111.23–1111.35 m (from Ma et al., 2006).

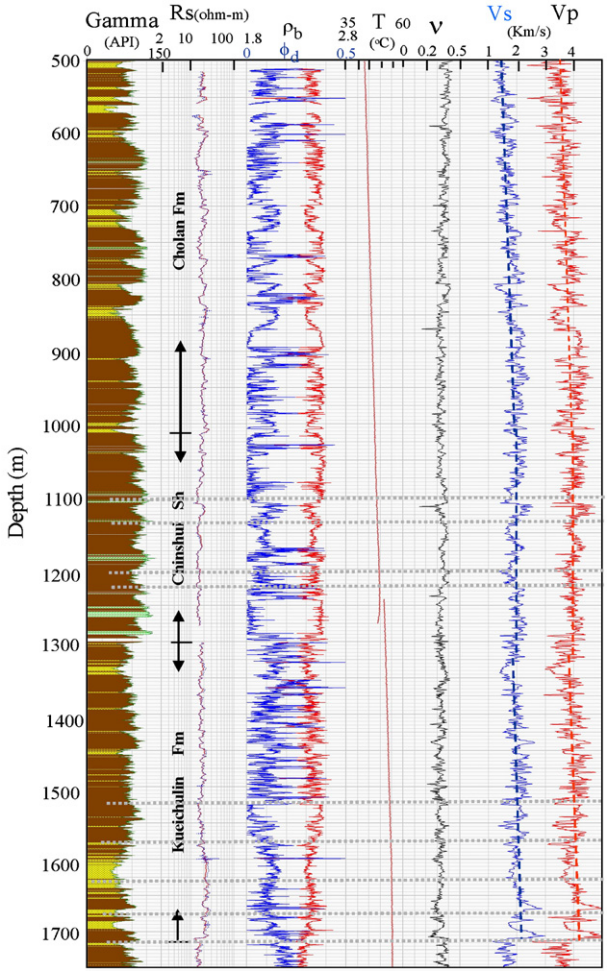

Fig. 5. Down-hole physical-property logs in hole-A between 500 and 1750 m. Track 1 is lithology column determined from gamma-ray log. Other tracks from left to right include: resistivity, density and density-derived porosity, temperature, Poisson ratio, shear- and P-wave velocities. Dashed lines on the sonic velocities indicate gross trends with depth. Locations of fault zone are marked in dashed lines.

FZ1111, and there is no hanging-wall breccia or entire breccia of any kind in FZ1712 and FZ1785, respectively. Furthermore, assuming the thickness of fault gouge is proportional to the amount of displacement along the fault, two major fault zones, FZ1111 and FZ1712 are the main slip zones on which repeated earthquakes have occurred (detailed analysis of FZ1111 see Ma et al., 2006).

3. Rock physical properties from down-hole logging

A comprehensive suit of geophysical logs was collected in hole-A from a depth of 500 m to 1750 m. P- and S-wave sonic velocity, gamma ray, electrical resistivity, density and temperature were recorded at a 15 cm sampling interval. Electrical image logs (FMS/FMI) are also acquired in both hole-A and hole-B to facilitate the analysis of fractures and faults intersected by the borehole as well as stress-induced wellbore failures (borehole breakout). The hole-deviation is less than 4° above depth 1600 m but gradually increase downward to 14° at depth 1865 m (see Fig. 3). Hole-drift was not measured below 1865 m but is believed to be greater than 14°. Well log data are identified by wire-line depths, whereas drilling depths are used in core data. Depth calibrations among cores and different log data have been made (see Hung et al., 2007; Lofts and Bristow, 1998; Major et al., 1998), and on average, the drilling depth is about 2 m deeper than the measured shown in Fig. 3 using the rig floor as a common datum.

Gamma-ray radiation, formation resistivity, density and density-derived porosity are primarily dependent on the formation lithology (Fig. 5). Variations in gamma-ray radiation are associated with the presence of clay minerals. The gamma-ray log in sandstones of the Cholan Formation show a typical upward decrease of radiation and corresponding an upward increase in both grain size and sandstone/shale ratio in the core. Overall, sandstone has higher resistivity, higher porosity and lower density with respective to shale. Transient mud temperature ($\pm 10^{-3}$ °C) in the intervals 500–1275 m and 1275–1842 m shows a relatively low gradient of 9 °C/km and 7 °C/km, respective. Although no thermal anomaly was observed due to circulation of mud immediately after the drilling, Kano et al. (2006) reported a slight heat signal around FZA1111 during repeated temperature measurements 6 months after the completion of drilling.

Velocity logs show an overall slight increase in both P- and S-wave sonic velocity with depth in the Cholan and Kueichulin Formations but constant in the Chinshui shale with values of 3.99 km/s (V_p) and 1.95 km/s (V_s). Both P- and S-wave data show relatively low velocity in both sandstones and some fault zones with intense fracturing. The V_p/V_s ratio has an average value of 2.08 (equivalent to a Poisson's ratio, ν, of 0.35) but can reach up to 2.4 ($\nu = 0.4$) in highly fractured fault zone. An abrupt change of physical properties occurred across FZ1712, below which values of resistivity, density and sonic velocities (V_p and

Table 3
List of calculated breakdown pressure (P_b), instantaneous shut-in pressure (P_s) in subsequent cycles of pressurization, reopening pressure (P_r) and tensile strength of rocks (T_o) measured from leak-off test at four depth intervals (note: water density of 1.1 g/cm^3 was used to calculate hydrostatic pressure, P_p)

Depth (m)	Breakdown		Shut-in P. 1, 4		Shut-in P. 2		Shut-in P. 3		Reopen	To
	P_b	Flow	P_s	Flow	P_s	Flow	P_s	Flow	P_r	P_b–P_r
	(MPa)	(l/min)	(MPa)	(l/min)	(MPa)	(l/min)	(MPa)	(l/min)	(MPa)	(MPa)
1279.6	24.2	15	19.4	15	19.6	15	19.5	15	24.2	0
			19.6	15						
1085.0	31.3	15	23.5	15	23.8	15	22.9	15	23.9	7.4
1179.0	17.7	16	16.8	16	16.2	Leak	13.9	Leak	17.4	0.3
1019.5	16.9	15	16.3	16	16.3	16	16	16	16.4	0.5

V_s) are significantly reduced by 50%, 3%, 18% and 25%, respectively. The drastic change of physical properties provides independent evidence that FZ1712 is also a formation boundary. Most fault zones are characterized by relatively low resistivity and density, and high Poisson's ratio (Fig. 5). FZ1111 displays the following unique characteristics: 1) the breccia zone has the lowest resistivity value in the borehole, about 40% less than adjacent host rocks; 2) low density, V_p and V_s (20–25% reduction), but V_p/V_s ratio (~2.4) and Poisson's ratio (~0.4); 4) low energy and velocity anisotropy, and fluid mobility (a proxy of permeability) in the massive gouge zone (in DSI log, see the following section); 5) anomalously high discharge of formation gas (Yang et al., 2005).

4. *In situ* stress state

4.1. Hydraulic fracturing

A standard commercial procedure of open-hole, extended leak-off tests (see Engelder, 1993) were conducted in hole-B at depths between 940 and 1350 m to determine *in situ* magnitudes of maximum (S_{Hmax}) and minimum (S_{hmin}) horizontal stresses. Dual straddle packers connected by tubing pipes were used to isolate an interval of the wellbore, and fluid was pumped into the open-hole section between the upper and lower packers. We apply fresh water to pressurize the intervals with several pressurization–depressurization cycles, and record the injection pressure, flow rate (including total flow) using surface pressure gauges (50 and 20 MPa) with accuracy of 0.4 MPa and electromagnetic flow-meters, respectively.

Assuming that the rocks surrounding the borehole are homogeneous, isotropic and elastic material, fracture-initiation takes place at the point of wellbore wall where maximum compressive stress acts (σ_θ=0°). The fluid pressure at the initiation of hydraulic fracture in an unfractured wellbore is the breakdown pressure (P_b) and is related to the tensile strength of the host rock (T_o) and formation fluid pressure (P_p) through the following equation (Zoback et al., 2003; Pollard and Fletcher, 2005):

$$P_b = \sigma(\theta = 0°) - P_p + T_o. \quad (1)$$

In the case of TCDP wells, the formation fluid pressure (P_p) measured in the wellhead of hole-A is nearly hydrostatic from surface to 1300 m. The greatest circumferential tensile stress (σ_θ) at the location (θ=0°) subjecting to remote biaxial compression, maximum horizontal stress axis (S_{Hmax}) and the minimum horizontal stress axis (S_{hmin}) is equal to $3S_{hmin}-S_{Hmax}$, and Eq. (1) can be expressed as:

$$P_b = 3S_{hmin} - S_{Hmax} - P_p + T_o. \quad (2)$$

During subsequent cycles of repressurization and reopening of the crack, the instantaneous shut-in pressure (P_s) is the fluid pressure at the crack tip. The hydraulic fracture is propagated normal to the minimum horizontal stress (S_{hmin}) such that P_s is usually equal to S_{hmin}:

$$S_{hmin} = P_s. \quad (3)$$

Provided tensile strength of the fractured surface is negligible (T_o=0), the reopening pressure (P_r) is the pressure necessary to keep circumferential stress slightly above zero. From the second (and subsequent) cycles of fluid injection we can get

$$S_{Hmax} = 3P_s - P_p - P_r. \quad (4)$$

Alternatively, if the borehole wall follows the uniaxial tensile failure criterion, this implies in-situ formation tensile strength (T_o) can be estimated by:

$$T_o = P_b - P_r. \quad (5)$$

Successful leak-off tests have been done at 4 locations of hole-B– 1279.6, 1179.0, 1085.0 and 1019.5 m– with two above and two below the FZ1137 (equivalent to FZ1111 of hole-A). In each run the packer was set at 10 MPa with constant flow rate of 10ℓ/min. At later stages of reopening tests, change of flow rate was applied to see its effects on P_s. At locations of 1019.5 m and 1085.0 m, clearly breakdown pressures, 6.5 MPa and 19.5 MPa, respective, are observed in the first cycle, and consistent P_s and P_r are recorded in subsequent repeated reopening test cycles (see Table 3 and Fig. 6). Calculated breakdown pressures at 1179.0 m and 1019.5 m are relatively low (17.7 MPa and 16.9 MPa), and leakage occurs in the subsequent cycles of fluid injection at 1179.0 m. Values of the first cycles test, 16.8 MPa and 16.3 MPa, were chosen to be the representative P_s for above two depths. Presumably, the leakage could be caused by reopening preexisting natural fractures and/or nucleated fractures propagating out the annulus between the packers and borehole wall in both tests. Estimated S_{Hmax} and S_{hmin} range between 32–35 MPa and 17–20 MPa, respectively, and do not vary much with depth except at 1085 m, where relatively higher value of 46 MPa (S_{Hmax}) and 23 MPa (S_{hmin}) were measured.

Given the depth of overburden, we can calculate the vertical stress from integration of density logs and plot with formation pore pressure (assume hydrostatic) (Fig. 7). Magnitudes of S_{hmin} and S_{Hmax} in each leak-off test can be calculated from Eqs. (3) and (4). There are two important features to note about the measured stress values at depth. First, the measurements can vary depending on the homogeneity of formation. For instance, the indurate homogeneous shale at 1085 m has higher S_{hmin} and S_{Hmax} than the other three locations with inter-laminated siltstone or shale. Similarly, mechanical experiments in the laboratory show much higher uniaxial compressive strength in above shale (~70 MPa) than the porous sandstone (8–11 MPa). Second, in all measurements S_{Hmax} is greater than the vertical stress which is, in turn, greater than S_{hmin} indicating a strike-slip fault regime in this area after the Chi-Chi earthquake.

4.2. Wellbore failure

Failure around the wall of a well could occur due to unequal horizontal stresses reaching the rock strength. There are two kinds of failure around the borehole wall: compressive shear failure in the area of maximum compressive circumferential (or hoop) stress (at the azimuth of S_{hmin}) and tensile failure in the

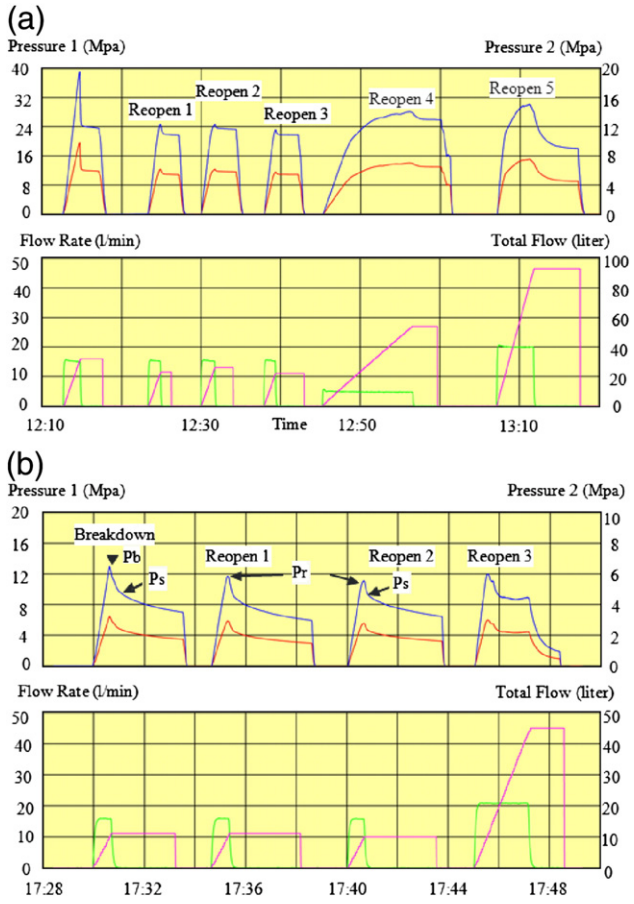

Fig. 6. Pressure–time (upper) and flow rate-time (below) curves from tests of (a) 1085.0 m and (b) 1019.5 m. Pressure is measured using two scales of sensors. Flow rate and total flow are represented by green and pink curves, respective. In both cases the instantaneous shut-in pressures (P_s) appear with good repeatability in cycles of tests. Points of breakdown pressure (P_b), instantaneous shut-in pressure (P_s) and reopening pressure (P_r) are shown in the pressure-time curves. Inverse proportion of P_s to flow rate is shown by change of flow rate in reopening tests.

area of the minimum compressive stress (at the azimuth of S_{Hmax}). Borehole breakouts are associated with the compressive failure so that the wellbore is no longer circular and elongated in the zone of failure. The borehole shape can be measured either by caliper measurement or image tools so that the azimuth of the greatest borehole diameter can be recorded. On the other hand, drilling-induced tensile fractures (DTFs) are formed due to overbalanced mud weight with formation pore pressure and can be observed from image logs. The origin of these two kinds of failure is closely related to the S_{Hmax} and S_{hmin} stress direction around the borehole, and thus, determining the orientation of fracturing zones can be used to infer *in situ* stress orientation (Suppe, 1985; Engelder, 1993, Zoback et al., 1985; 2003).

Breakouts appear in dark bands of low reflectance in the opposed sides of the enlarged borehole wall on the logs of formation MicroScanner (FMS) or formation MicroImager (FMI) developed by Schlumberger (Plumb and Hickman, 1985; Zoback et al., 2003). Both the orientation and opening angle (width) of the breakouts can be read straightforwardly from dark-paired bands (Fig. 8a). The DTFs (Fig. 8b) consist of two small inclined parallel fractures that show en echelon pattern and macroscopically make up longitudinal fractures parallel to the borehole axis. Tensile fractures on opposite sides of the wall are often oriented 90° from the mid-points of the wellbore breakouts (Zoback et al., 2003). The depth ranges of acquired borehole images include FMS, 508–1250 m in hole-A, and FMI, 1250–1865 m in hole-A and 932–1338 m in hole-B. Among them, the quality of images in hole-A is poor below 1750 m due to deviated trajectories and washouts of the borehole. Breakouts above 700 m are less developed or not detected by FMS due to only 50% coverage in borehole of 16 cm diameter. Intervals with no borehole failure may be due partly to insufficient coverage of borehole wall and/or to the dependence of borehole failure on rock strength, depth, stress state and mud density (Engelder, 1993). Typical observed breakouts are 0.5–4.2 m long and 0.5–2 cm wide, and DFTs range 0.5–3 m long and 0.2–0.5 cm thick.

Orientations of the S_{Hmax} determined from breakouts and DTFs in the section of 700–1700 m compiled from hole-A and hole-B are shown in Fig. 8c (orientation of breakouts is shifted 90° as they form at the azimuth of S_{hmin}). Breakouts and tensile fractures form roughly 90° apart, as predicted by the theory, and borehole failure is dominated by breakouts due to under-balanced mud weight. Breakouts are also relatively better developed, and data scattering is smaller, in the Kueichulin Formation than other locations above it. A significant change in the average S_{Hmax} azimuth appears across the depth about 1300 m (also a stratigraphic boundary between the Chihsui shale and Kueichulin Formation). The S_{Hmax} oriented in 103°–138° with an average of 123° in the section of 700–1300 m as opposed to 137°–164° (154° on average) from 1300 m to 1700 m. Apparently, the azimuth decoupling of S_{Hmax} could be

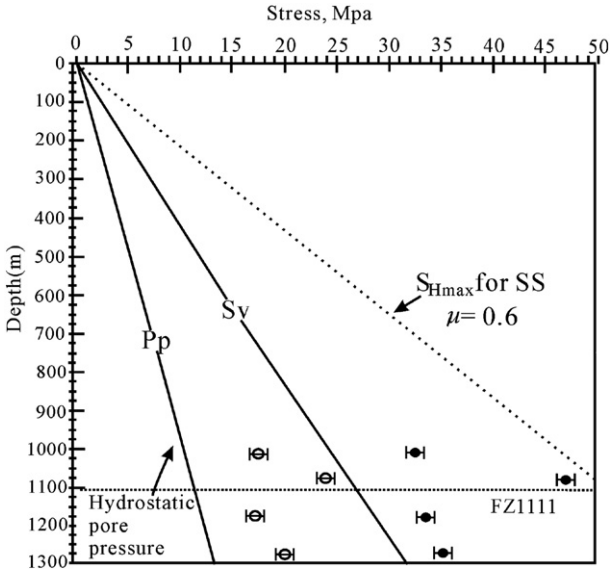

Fig. 7. Plot of overburden stress (S_v) from integration of density logs, hydrostatic pore pressure, and S_{Hmax} (filled symbol) and S_{hmin} values (open symbol) determined from leak-off tests at different depths. Dotted line shows the location of FZ1111. Heavy dashed line indicates the upper limit of the stress magnitude for a strike-slip fault stress regime based on Eq. (6) and coefficient of friction μ=0.6.

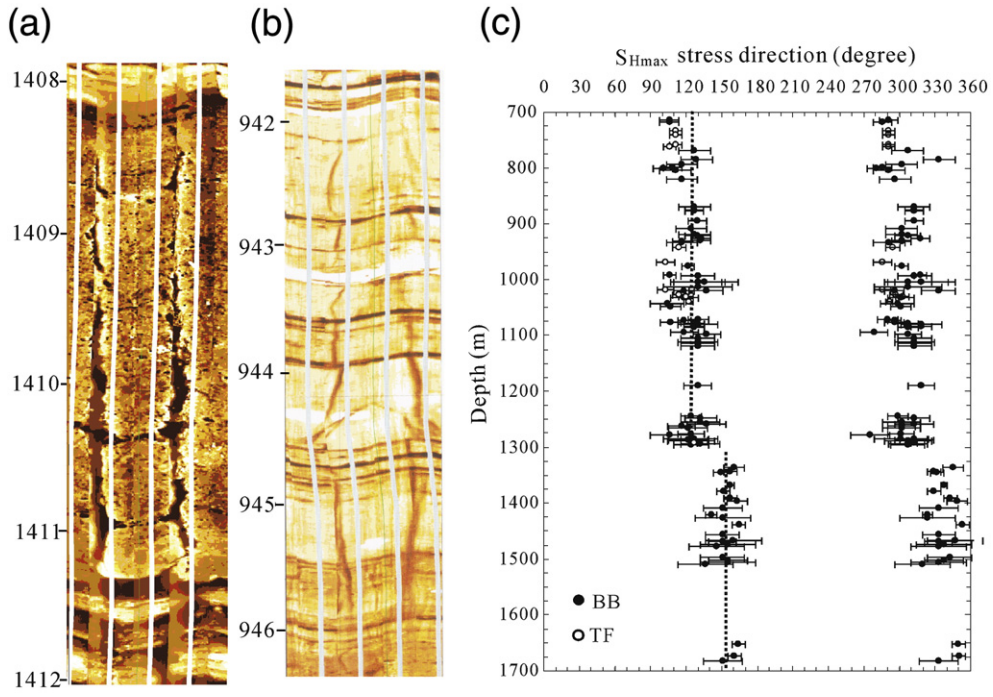

Fig. 8. (a) Borehole breakouts as dark bands in opposite sides of the wellbore wall in FMI image logs of hole-A between 1409 and 1411 m, and (b) drilling-induced tensile fractures in the hole-B between 941 and 947 m. (c) The plot of azimuth of S_{Hmax} determined from breakouts (BO) and tensile fractures (TF) in the TCDP wells. Width of bar shows an opening angle of BO and TF with dark and open circles, respectively, as mid-point. Dotted lines are average of mid-points between sections of 700–1300 m and 1300–1700 m.

associated with the change of rock type from massive sandstone and mudstone dominated Cholan Formation and Chinshui Shale, respective to common mudstone/siltstone layered Kueichulin Formation. Last, the S_{Hmax} within the depth interval of leak-off tests (1019–1280 m) is oriented between 104° and 138° (average 124°) and shows a consistent azimuth of 130° in

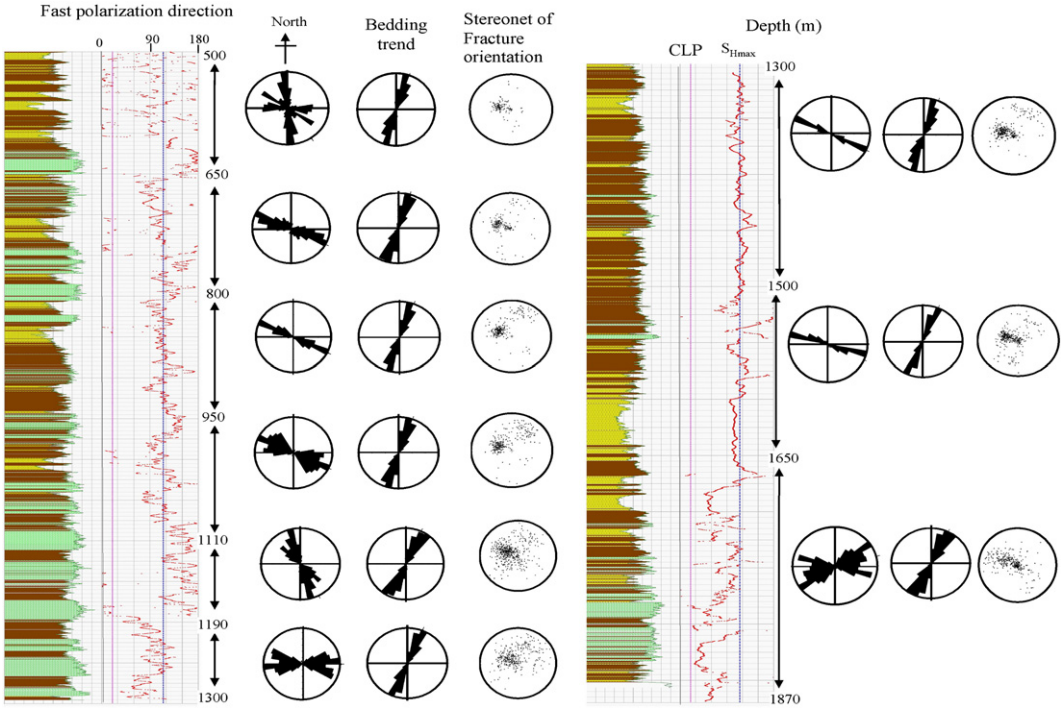

Fig. 9. Comparison of the fast-shear polarization direction (shown in scatter plot and 9 discrete zones) with bedding trend determined from borehole images and fracture orientations measured from core images. Azimuths of the Chelungpu fault (CLF, 20°) and maximum horizontal principal stress (S_{Hmax}, 115°) determined from earthquake focal mechanisms in central western Foothills of Taiwan (Yeh et al., 1991) are shown for references.

the vicinity of FZ1111. To the first order, they are parallel to the direction of convergence between the Philippine and Eurasian plates derived from GPS measurement (Yu et al., 1997).

4.3. Shear seismic wave anisotropy

Shear waves propagating through microcracks or planar fabrics can develop polarized orthogonal components of fast wave in the stiff direction and slow wave in the compliant direction that separate in time (Crampin and Lovell, 1991). If the stress difference is large enough to close the cracks in one orientation, it is suitable to use shear-wave splitting to determine in-situ stress orientation. Data from Dipole-Shear Sonic Imaging (DSI) logs (mark of Schlumberger) acquired over an interval of 508–1870 m in hole-A were used to assess shear-wave velocity anisotropy. The DSI tool consists of monopole (P- and S-mode) and cross dipole sources at relatively low frequencies (0.8–5 kHz) and receiver arrays 15 cm apart (vertical resolution). The shear waves cause a flexing of the borehole wall, which in turn excites shear waves penetrating approximately 1.5 m into the formation at a shear velocity of 1.5 km/s (Schlumberger, 1995). Three measurements of computed anisotropy – energy anisotropy, slowness anisotropy and time anisotropy – can be used to indicate the strength of anisotropy (Brie et al., 1998). Large energy difference between the maximum and minimum values of fast- and slow-shear waves, especially when minimum energy is low, indicate zones of significant anisotropy. Other factors such as curved borehole trajectory and/or irregular borehole size such as occurred below 1750 m in hole-A could also generate anomalous high minimum energy and cause an artifact in anisotropy.

Zones of significant anisotropy, with low minimum energy and difference between maximum and minimum energy over 50%, are prevalent in the Kueichulin Formation from the DSI log. Conversely, the energy difference, thickness and frequency of significant anisotropy are relatively less in the Cholan Formation (both the hanging-wall and footwall of the Sanyi thrust) than in both the Chinshui Shale and Kueichulin Formations. The overall uncertainty of fast-shear azimuth is also related to the degree of shear anisotropy, which ranges between ±15° and ±2° in weak and strong anisotropic rocks, respective. Results of analyses at depth intervals of 508–1870 m are shown by both scatter plots and rose diagrams of 9 discrete intervals of similar orientations of fast shear-wave polarization (Fig. 9). Bedding trend and low-hemisphere stereo projection of fracture orientation are also shown at the same depth interval for comparison. In all lithologic units the bedding planes strike nearly parallel to the average trend of the Chelungpu fault. Fracture orientations appear to be randomly distributed except in the section below 1650 m where bedding fractures are commonly observed.

Except in a few depth zones, such as 500–650 m, 738–770 m, 785–815 m, 1517–1547 m, and 1650–1870 m, where dispersive orientations coupling with high minimum energy and low energy anisotropy appear, a prominent NW–SE fast-shear polarizing direction was generally observed. Particularly, a very consistent mean direction with small dispersion of 115°±1°–2° (95% confidence interval) appears in the strongly anisotropic Kueichulin Formation at 1300–1650 m in both sandstone and siltstone/shale interlayer. Relatively consistent fast-shear polarization directions appear across FZ1111 (ranging 156°–174° between 1105 and 1115 m) compared to the interval of 1078–1190 m with trending in a much broad range of 130°–170° (Fig. 9). Thus, to the first order, there is no observable systematic change of trend on fast-shear polarization across the Chi-Chi slip zone.

The overall NW–SE trending fast-shear polarization is normal to subnormal to the bedding strike. Besides the predominant fast-shear azimuth of 115°, other subdirections occurred in 153°±5° (500–650 m and 1078–1190 m) and 90°±5° (500–650 m and 1190–1295 m), 75°±4° (1650–1870 m) are also observed. The two subsets of orientation (153° and 90° are geometrically formed as conjugates with respect to the main orientation of 115°. This mean direction of 115° is in good agreement with direction of regional maximum horizontal principal stress deduced from earthquake focal mechanisms by Yeh et al. (1991) and the direction of secular crustal motion (Yu et al., 2001) in western central Taiwan.

The relationship between anisotropy of P-wave velocity and rock petrofabrics using sandstone samples collected from TCDP cores was studied by Louis et al. (2005). Their results showed that the anisotropy of P-wave velocity can be explained by the presence of preferred alignment of microcracks with a mean azimuth of 105° (85°–130°). Considering measurement errors and different scales of observation in two studies of velocity anisotropy, there is a coherent orientation of both fast P-wave and S-wave polarization. Although preferentially aligned microcracks in the thin sections can account for the P-wave anisotropy measured in core sample, the randomly oriented macroscopic fractures and faults cannot be the explanation for the shear-wave anisotropy measured in the borehole. Other possible mechanisms are discussed in the following.

5. Discussion

We have characterized the subsurface structure, and physical properties of formation and fault zones, in-situ stress in the TCDP boreholes through core studies, down-hole geophysical measurements and hydrofracturing experiments. Essential features of individual category have been illustrated in the previous sections. In this section we provide interpretation on the origin of subsurface structure and the causes that could affect the anisotropy of shear-wave velocity. An further extension study of the stress state after the Chi-Chi earthquake is also marked. We also discussed the composite characteristics of the Chi-Chi rupture zone including fabrics, clay minerals, physical properties and thermal anomalies and their implications on the dynamic weakening mechanisms.

A drastic change of regional dip occurs across the Sanyi main thrust (FZ1712) from rather uniform to steep dip. The appearance of both steep to overturned beds and thrust faults underlying the Sanyi thrust (Fig. 2) is contrary to the observation of normal faults in the structural position 15 km to the north of the drill site (Hung and Wiltschko, 1993, their Fig. 12). The extent of the contractional deformation beneath the Sanyi thrust is not known, nor is the boundary between the two structural styles. However, because the steep beds observed in the well do not crop out, the extent of the subthrust fold must be limited. We interpreted it as the overturned forelimb of

a fault-propagation fold formed in front of the Sanyi thrust, later broken through along the anticlinal axial surface. Thrust displacement with erosion has removed the hanging-wall anticline. Another plausible alternative is that this anticline is a hanging-wall imbricate of the underlying Changhua thrust.

From comparison of the anisotropy of shear-wave velocity and earthquake focal mechanism, we have shown that there is, in general, a good agreement in orientations between fast shear-wave polarization and regional maximum horizontal stress, particularly within the strong anisotropic Kueichulin Formation. Nevertheless, there are several causes of shear-wave anisotropy in sedimentary rocks (e.g., Crampin and Lovell, 1991; Esmersoy et al., 1995; Boness and Zoback, 2004, 2006): 1) anisotropy due to layering (bedding planes) in sedimentary rocks (Fig. 10a); 2) anisotropic *in situ* stresses that cause the preferred closure of microfractures and generate a fast direction parallel to the regional maximum horizontal stress (S_{Hmax}); 3) alignment of macrofractures (Fig. 10b); 4) dilatancy of stress-aligned fluid-filled microcracks that produce the fast direction parallel to S_{Hmax}; 5) alignment of minerals or grains (Fig. 10c); and 6) borehole shape or azimuth of borehole elongation (Brie et al., 1998).

Because the shear-wave anisotropy displays a preferred orientation, the observed the random orientation of macroscopic fractures and faults in hole-A (Fig. 9) cannot be the explanation. Alignment of mineral grains or fluid-filled dilatational microcracks in bedded sandstone is unlikely since no preferred orientations of minerals or veins were observed either on the cores or thin sections. Esmersoy et al. (1995) reported that there is little effect on shear anisotropy for vertical wells (or vertical propagation of shear wave) in layered beds with dip less than 30°–40°. A similar result was shown here that the strike of sedimentary beds or faults does not impose correlated effects since distinct different directions between the fast shear-wave and trend of the Chelungpu fault or beds. On the other hand, shear waves propagating through steep beds will split (as shown in Fig. 10c). Consequently, the NE–SW trend of fast-shear polarization below 1712 m could be due to this effect. Other factors such as enlarged borehole size, irregular shape (rugosity) and deviated trajectory (8°–15°) may also contribute the azimuth dispersion of the fast shear-wave in this depth range.

Anisotropy could also be induced by elongation of borehole (borehole ovality) in that the flexural wave is polarized fast along the short axis and slow along the large axis. An open-hole six-arm caliper log (EMS, mark of Schlumberger) was collected in hole-B at an interval of 933–1345 m. Among over 400 data of best-fit hole ellipse with ratio of long-axis and short axis greater than 1.10, the mean populated azimuth of short axis is orientated 163° but with a large dispersion of 13° (95% confidence interval). Compared with the DSI results, it can be concluded that the borehole ovality does not control the dominant orientation of the fast-shear polarization.

The in-situ stress state measured at the drill site 6 years after the Chi-Chi earthquake shows a nearly strike-slip fault regime. Presumably a thrust-fault stress regime would exist prior to the Chi-Chi earthquake, but without detailed stress information it is not known how the stress state changed. Alternatively, we can use the measured stress condition to evaluate reactivation potential on the Chelungpu fault. In a vertical well we can estimate S_{Hmax} if the pore pressure, overburden pressure (S_V) and S_{hmin} are known. Without excessive mud weight and mud cooling, assuming measured S_{Hmax} and S_{hmin} correspond to the maximum (S_1) and minimum (S_3) principal stresses, the upper-bound (critically stressed) theoretical value of S_{Hmax} for a

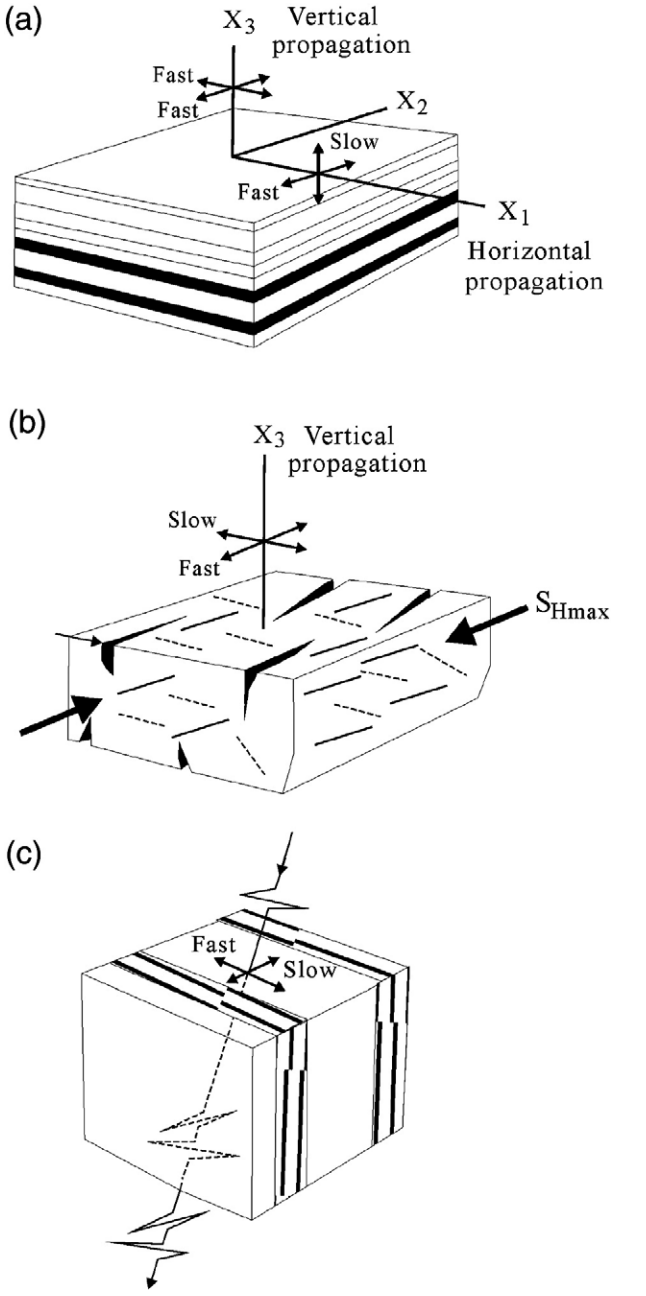

Fig. 10. Three basic types of anisotropy associated with shear-wave propagation. (a) Transverse isotropy with a vertical axis of symmetry associated with fine layering of shale with horizontal bedding for vertically and horizontally propagating shear wave. (b) Transverse isotropy with a vertical axis of symmetry caused by either stress-induced anisotropy as a result of preferential closure of fractures (dashed lines) in a randomly fractured rocks or alignment of macrofractures. (c) Structural isotropy as a result of planar features such as fabrics within fault zones, bedding planes or alignment minerals/grains (modified from Boness and Zoback, 2006).

strike-slip environment is constrained by Anderson's faulting theory and is given by (Zoback et al., 2003):

$$S_{\mathrm{Hmax}} = \left(S_{\mathrm{hmin}} - P_{\mathrm{p}}\right)\left[\left(1+\mu^2\right)^{1/2}+\mu\right]^2 + P_{\mathrm{p}}. \quad (6)$$

Applying values of hydrostatic pore pressure, S_{hmin} values (24 MPa) from leak-off tests and assuming static coefficient of friction $\mu=0.6$, the estimated S_{Hmax} with depth is shown in Fig. 7. The upper-bound value of theoretical S_{Hmax} (49.6 MPa) is close to the measured S_{Hmax} (46.3 MPa) at 1085 m, which indicates that faults at this depth could be reactivated in strike-slip motion if μ is smaller than 0.6. To further study this problem, additional factors need to be considered, such as that the measured S_{Hmax} should be modified by 3-D strength criterion (e.g., Haimson and Song, 1993; Lee and Haimson, 1993) that includes effects of fluids, vertical and radial stresses, and anisotropy of rocks.

Formation physical properties show consistent relationship with either depth or lithology. P- and S-wave velocity and temperature, in general, increase with depth; whereas gamma ray, resistivity, density and density-derived porosity are primarily dependent on the lithology. Among all fault zones, FZ1111 displays the lowest resistivity in the well, low density, V_{p} and V_{s}. The low resistivity is a result of infiltration of mud into highly fractured breccia based on core examination, and the low density, V_{p} and V_{s}, along with high $V_{\mathrm{p}}/V_{\mathrm{s}}$ and Poisson's ratio in the gouge zone are attributable to large amounts of clay and/or fluid. Mineralogical analyses also show relatively high amount of smectite and smectite/illite ration in FZ1111 compared to other fault zones (Kuo et al., 2005). Because smectite, upon heating, easily transforms into illite or smectite/illite mixed layer (Ho et al., 1999), the abundant smectite provides further evidence that FZ1111 was the slip zone during the Chi-Chi earthquake.

In spite of large surface displacements, no temperature anomaly was observed at FZ1111, and nearly hydrostatic fluid pressure was measured. Nevertheless, small positive amplitudes of heat anomaly were reported, 0.1 °C in the shallow pilot hole (450 m deep) drilled near the Fengyuan city (Tanaka et al., 2006) and 0.06 °C in hole-A measured after the drilling (Kano et al., 2006). Applying above heat anomalies, the calculated apparent (or dynamic) coefficients of friction, $\mu=0.12$–0.13 in the former and 0.04–0.08 in the latter, are extremely low compared the static coefficient of friction determined in the laboratory, 0.6 to 0.7 (Byerlee, 1978) or 0.35 to 0.5 for shale (Morrow et al., 1992). These results also indicate low resolved shear stress (~1 MPa) and low frictional heat on the slip zone. If the above estimates are applicable to localized fault patch, it indicates that there are dynamic mechanisms that reduce the frictional strength, such as mechanical lubrication, frictional melting or thermal fluid pressurization. The small value of heat implies melting probably did not occur and explains few microscopic textures of melting in the gouge layer. Furthermore, even if hydrostatic pressure was observed at the wellhead, without down-hole *in situ* measurement, it is difficult to evaluate if the overpressurized pore pressure and/or mechanical weakening operate during faulting process. Abnormal high pore pressure can be generated in frictional experiments using clay gouge in FZ1111 of low permeability between 10^{-14} m^2 and 10^{-17} m^2 (Sone et al., 2005). The high water content and smectite-rich clay gouge is suitable for mechanical weakening (Wu, 1978; Chester et al., 1993; Wintsch et al., 1995) during faulting of the Chi-Chi earthquake.

6. Conclusions

The major scientific goal of the TCDP boreholes is to understand the physical mechanism involved in the large displacement during the Chi-Chi earthquake. We have attempted to answer this and relevant questions through studies of subsurface structure, fault-zone fabrics, formation physical properties and in-situ stress state. Consistent correlations among fault-zone fabrics, physical properties and clay mineralogy enable us to identify the bedding-parallel fault zone at depth 1111 m in hole-A being the rupture fault. The 2-cm wide, ultra-fine-grained and foliated clay gouge near the bottom of the FZ1111 is interpreted to be the slip zone during the Chi-Chi earthquake. Ancillary investigation of temperature signal around the FZ1111 suggests that the slip zone is low frictional strength with both low coefficient of friction and low shear stress. This result is consistent with the first order observation of no systematic change of maximum horizontal stress orientation deduced from borehole failure and shear-wave anisotropy. With the aid of detachment fault within the Chinshui Shale, dynamic fault weakening mechanisms such as mechanical lubrication and thermal pressurization may operate during faulting process and result in rapid motion and large coseismic displacements in the Chelungpu fault segment.

Acknowledgements

We are grateful to all the participants of TCDP including project principal investigators, international collaborators from USGS, Stanford University, JAMSTEC, and universities and research institutes in Japan, and field assistants and students from NCU and NTU. Funding of the TCDP is primarily from National Science Council (NSC), R.O.C. We thank the International Continental Scientific Drilling Program (ICDP) for providing partial fund and technical consult. Comments and suggestions from David Wiltschko and an anonymous reviewer help us greatly improve this manuscript. This research was supported by the Taiwan Earthquake Research Center (TEC) funded through National Science Council (NSC) with grant number NSC93-2119-M-008-019 and NSC94-2119-M-008-009 JH. The TEC contribution number for this article is 00021.

References

Blanpied, M.L., Marone, C.J., Lockner, D.A., Byerlee, J.D., King, D.P., 1998. Quantitative measurement of the variation in fault rheology to fluid–rock interactions. J. Geophys. Res. 103, 9691–9712.

Boness, N., Zoback, M., 2004. Stress-induced seismic velocity anisotropy and physical properties in the SAFOD pilot hole in Parkfield, CA. Geophy. Res. Lett. 31, L15S17.

Boness, N., Zoback, M., 2006. A multiscale study of the mechanisms controlling shear velocity anisotropy in the San Andreas Fault observatory at depth. Geophysics 71 (5), F131–F146.

Brie, A., Endo, T., Hoyle, D., 1998. New directions in sonic logging. Oilfield Review 10, 40–55.
Byerlee, J.D., 1978. Friction of rocks. Pure Appl. Geoph., 116, 615–629.
Chang, S.S.L., 1971. Subsurface geologic study of the Taichung basin, Taiwan. Petrol. Geol. Taiwan 8, 21–45.
Chester, F.M., Evans, J.P., Biegel, R.L., 1993. Internal structure and weakening mechanisms of the San Andreas Fault. J. Geophys. Res. 98, 771–786.
CPC (Chinese Petroleum Corporation), 1982. Geologic map of western Taiwan, Taichung sheet (1: 100,000). TPED, CPC, Miaoli, Taiwan.
Crampin, S., Lovell, J., 1991. A decade of shear-wave splitting in the Earth's crust: what does it mean? What use can we make of it? And what should we do next? Geophys. J. Int. 107, 387–407.
Dominguez, S., Avouac, J.P., Michel, R., 2003. Horizontal coseismic deformation of the 1999 Chi-Chi earthquake measured from Spot satellite images: implications for the seismic cycle along the western foothills of central Taiwan. J. Geophys. Res. 108 (B2), 2083. doi:10.1029/2001JB000951.
Engelder, T., 1993. Stress Regimes in the Lithosphere. Princeton university press, Princeton, New Jersey. 457 pp.
Esmersoy, C., Kane, M., Boyd, A., Denoo, S., 1995. Fracture and stress evaluation using dipole-shear anisotropy logs. SPWL Symp. Trans., 36th. 12 pp.
Haimson, B., Song, I., 1993. Laboratory study of borehole breakouts in Cordova Cream: a case of shear failure mechanism. In: Haimson, B.C. (Ed.), 34th US Rock Mechanics Symposium, Madison, Wisconsin, pp. 1047–1056.
Heermance, R.V., Shipton, Z.K., Evans, J.P., 2003. Fault structure control on fault slip and ground motion during the 1999 rupture of the Chelungpu fault. Bull. Seis. Soc. Am. 93, 1034–1051.
Hickman, S., 1991. Stress in the lithosphere and strength of active faults, U.S., Nat. Rep. Int. Union Geo. Geophys., 1987–1990. Rev. Geophys. 29, 759–775.
Hirono, T., Ikehara, M., Otsuki, K., Mishima, T., Sakaguchi, M., Soh, W., Omori, M., Lin, W., Yeh, E.C., Tanikawa, W., Wang, C.Y., 2006. Evidence of frictional melting from disk-shaped black material, discovered within the Taiwan Chelungpu fault system. Geophys. Res. Lett. 33, L19311. doi:10.1029/2006GL027329.
Ho, N.C., Peacor, D.R., van der Pluijm, B.A., 1999. Preferred orientation of phyllosilicates in Gulf Coast mudstones and relation to the smectite–illite transition. Clay and Clay Min. 47, 495–504.
Huang, S.T., Wu, R.C., Hung, J.H., Tanaka, H., 2002. Sedimentary facies, stratigraphy and deformation structures of cores from Fengyuan and Nantou wells of the Chelungpu fault. Terr. Atmos. Ocean. Sci. 13 (3), 253–278.
Hubbert, M.K., Rubey, W.W., 1959. Role of fluid pressure in the mechanics of overthrust faulting. Bull Geol. Soc. Am. 70, 115–166.
Hung, J.H., Wiltschko, D., 1993. Structure and kinematics of arcuate thrust faults in the Miaoli–Cholan area of western Taiwan. Petrol. Geol. Taiwan 28, 59–96.
Hung, J.H., Suppe, J., 2002. Subsurface geometry of the Sanyi–Chelungpu faults and fold scarp formation in the 1999 Chi-Chi Taiwan Earthquake. EOS Trans. AGU 83 (47) Fall Meeting suppl. abstract T61B-1268.
Hung, J.H., Wu, Y.H., Yeh, E.C., TCDP Scientific Party, 2007. Physical properties, subsurface structure and fault zone characteristics in scientific drill holes of Taiwan Chelungpu Fault Drilling Project. Terr. Atmos. Ocean. Sci. TCDP spec. issue.
Isaacs, A., Evans, J., Song, S.R., Kolesar, P., 2007. Characterizing brittle deformation, damage parameters, and clay composition in fault zones: variations along strike and with depth in the Chelungpu Fault zone. Terr. Atmos. Ocean. Sci. TCDP spec. issue.
Kano, Y., Mori, J., Fujio, R., Ito, H., Yanagidani, T., Nakao, S., Ma, K., 2006. Heat signature on the Chelungpu fault associated with the 1999 Chi-Chi, Taiwan earthquake. Geophys. Res. Lett. 33, L14306. doi:10.1029/2006GL026733.
Kuo, L., Song, S., Chen, H., 2005. Characteristics of clay minerals in the fault zone of TCDP and its implications. EOS Trans. AGU 86 (52) Fall Meeting suppl. abstract. T43D-05.
Lee, M., Haimson, B., 1993. Laboratory study of borehole breakouts in Cordova Cream: a case for extensile failure mechanism. In: Haimson, B.C. (Ed.), 34th US Rock Mechanics Symposium, Madison, Wisconsin, pp. 1039–1045.
Lee, Y.H., Hsieh, M.L., Lu, S.D., Shih, T.S., Wu, W.Y., Sygiyama, Y., Azuma, T., Kariya, Y., 2003. Slip vectors of the surface rupture of the 1999 Chi-Chi earthquake, western Taiwan. J. Struct. Geol. 25, 1917–1931.
Lin, A.T., Wang, S.M., Hung, J.H., Wu, M.S., Liu, C.S., 2007. Stratigraphy and geology of the Taiwan Chelungpu-fault Drilling Project-A borehole and its neighboring region, central Taiwan. Terr. Atmos. Ocean. Sci. TCDP spec. issue.
Lofts, J., Bristow, J., 1998. Aspects of core-log integration: an approach using high resolution images. In: Harvey, P.K., Lovell, M.A. (Eds.), Core-Log Integration, Geologic Society, London, Spec. Pub. 136, pp. 273–283.
Louis, L., Christian, D., Robin, P., Wong, T.F., 2005. Anisotropy of magnetic susceptibility, and P-wave velocity in core samples from the Taiwan Chelungpu-fault Drilling Project (TCDP). Eos Trans. AGU 86 (52) Fall meeting suppl., abstract T51A-1319.
Ma, K.F., Song, T.R.A., Lee, S.J., Wu, H.I., 2000. Spatial slip distribution of the September 20, 1999, Chi-Chi, Taiwan, earthquake (Mw 7.6): inverted from teleseismic data. Geophys. Res. Lett. 27, 3417–3420.
Ma, K.F., Brodsky, E.E., Mori, J., Ji, C., Song, T.R.A., Kanamori, H., 2003. Evidence for fault lubrication during the 1999 Chi-Chi, Taiwan, earthquake (Mw 7.6). Geophys. Res. Lett. 30, 1244. doi:10.1029/2002GL015380.
Ma, K.F., Wang, C.Y., Hung, J.H., Song, S.R., Tsai, Y.B., Mori, J., Tanaka, H., Yeh, E.C., Sone, H., Kuo, L.W., Wu, H.Y., 2006. Slip zone and energetics of a large earthquake from the Taiwan Chelungpu-fault Drilling Project. Nature 444, 473–476.
Major, C., Pirmez, C., Goldberg, D., Leg 166 Scientific party, 1998. High resolution core-log integration techniques: examples from the Ocean Drilling Program. In: Harvey, P.K., Lovell, M.A. (Eds.), Core-Log Integration, Geol. Soc. London, Spec. Pub. 136, pp. 285–295.
MOEACGS, 2000. Report of Geological Investigation of 921 Chi-Chi earthquake. Ministry of Economic Affairs, Central Geol. Survey. 314 pp.
Mori, J., Ito, H., Wang, C.W., 2002. Chelungpu fault drilling could resolve seismological issues. EOS Trans. AGU 83 Fall Meeting suppl. p. 255.
Morrow, C., Radlney, B., Byerlee, J.D., 1992. Frictional strength and the effective pressure law of montmorrillonite and illite clays. In: Brace, W.F., Evans, B., Wong, T.F. (Eds.), Fault Mechanics and Transport Properties of Rocks. Elsevier, New York, pp. 69–89.
Noda, H., Shimamoto, T., 2004. Thermal pressurization and slip-weakening distance of a fault: an example of the Hanaore fault, southwest Japan. Bull. Seis. Soc. Am. 54, 1224–1233.
Plumb, R., Hickman, S., 1985. Stress-induced borehole elongation: a comparison between the four-arm dipmeter and the borehole televiewer in the Auburn geothermal well. J. Geophys. Res. 90 (B7), 5513–5521.
Pollard, D., Fletcher, R., 2005. Fundamental of Structural Geology. Cambridge University Press, pp. 234–239.
Rutter, E., Holdsworth, R., Knipe, R., 2001. The nature and tectonic significance of fault-zone weakening: an introduction. In: Holdsworth, R., Strachan, R., Magloughlin, J., Knipe, R. (Eds.), The Nature and Tectonic Significance of Fault Zone Weakening. Geol. Soc. London, Spec. Pub. 186, pp. 1–11.
Schlumberger, 1995. DSI "Dipole Shear Sonic Imaging". Oilfield Marketing Services, Schlumberger.
Scholz, C.H., 1998. Earthquakes and frictional laws. Nature 391, 37–42.
Scholz, C.H., 2002. The Mechanics of Earthquakes and Faulting. Cambridge Univ. Press, New York. 471 pp.
Sone, H., Shimamoto, T., Noda, H., Song, S., Ma, K., Hung, J., Wang, C., 2005. Frictional properties and permeability of fault rocks from Taiwan Chelungpu-fault Drilling Project and their implications for high-velocity slip weakening. EOS Trans. AGU 86 (52) Fall Meeting suppl. abstract. T43D-06.
Sone, H., Yeh, E., Nakaya, T., Hung, J.H., Ma, K.F., Wang, C.Y., Song, S.R., Shimamoto, T., 2007. Mesoscopic structural observations of cores from the Chelungpu fault system, Taiwan Chelungpu-fault drilling project Hole-A, Taiwan. Terr. Atmos. Ocean. Sci. TCDP spec. issue.
Suppe, J., 1985. Present-day stress directions in western Taiwan inferred from borehole elongation. Petrol. Geol. Taiwan 21, 1–12.
Suppe, J., Wittke, J., 1977. Abnormal pore-fluid pressures in relation to stratigraphy and structure in the active fold-and-thrust belt of northwestern Taiwan: petrol. Geol. Taiwan 14, 11–24.
Tanaka, H., Wang, C.Y., Chen, W.M., Sakaguchi, S., Ujiie, K., Ito, H., Masataka, A., 2002. Initial science report of shallow drilling penetrating into the Chelungpu fault zone. Taiwan. Terr. Atmos. Ocean. Sci. 13, 227–251.

Tanaka, H., Chen, W.M., Wang, C.Y., Ma, K.F., Urata, N., Mori, J., Ando, M., 2006. Frictional heat from faulting of the 1999 Chi-Chi, Taiwan earthquake. Geophys. Res. Lett. 33, L16316. doi:10.1029/2006GL026673.

Vrolijk, P., Van der Pluijm, B., 1999. Clay gouge. J. Struct. Geol. 21, 1039–1048.

Wang, C.Y., Li, C.L., Su, F.C., Leu, M.T., Wu, M.S., Lai, S.H., Chern, C.C., 2002. Structural mapping of the 1999 Chi-Chi earthquake fault, Taiwan, by seismic reflection methods. Terr. Atmos. Ocean. Sci. 13, 211–226.

Wang, C.Y., Li, C.L., Lee, H.C., 2004. Constructing subsurface structures of the Chelungpu fault to investigate mechanisms leading to abnormally large ruptures during the 1999 Chi-Chi earthquake, Taiwan. Geophys. Res. Lett. 31, L02608. doi:10.1029/2003GL 018323.

Wang, J.H., 2006. Energy release and heat generation during the 1999 M7.6 Chi-Chi, Taiwan earthquake. J. Geophys. Res 111. doi:10.1029/2005JB004018.

Wibberley, C.A.J., Shimamoto, T., 2005. Earthquake slip weakening and asperities explained by thermal pressurization. Nature 436, 689–692.

Wintsch, R.P., Christofferson, R., Kronenberg, A.K., 1995. Fluid–rock reaction weakening of fault zones. J. Geophys. Res. 100, 13021–13032.

Wu, T.F., 1978. Mineralogy and physical nature of clay gouge. Pageoph. 116, 655–679.

Yang, T., Walia, V., Lee, H., Song, S., Wang, C., 2005. Compositions of on-site monitoring on dissolved gas of drilling mud flow and pore-gases of drilled cores of TCDP. AGU 86 (52), Fall meeting suppl., abstract T51A-1315.

Yang, M., Rau, R.J., Yu, J.Y., Yu, T.T., 2000. Geodetically observed surface displacements of the 1999 Chi-Chi, Taiwan, earthquake. Earth Planets Space 52, 403–413.

Yeh, Y.H., Lin, C.H., Barrier, E., Angelier, J., 1991. Stress tensor analysis in the Taiwan area from focal mechanisms of earthquake. Tectonophysics 200, 267–280.

Yu, S.B., Chen, H.Y., Kuo, L.C., 1997. Velocity field of GPS stations in the Taiwan area. Tectonophysics 274, 41–59.

Yu, S.B., Kuo, L.C., Hsu, Y.J., Su, H.H., Liu, C.C., 2001. Preseismic deformation and coseismic displacements associated with the 1999 Chi-Chi, Taiwan, earthquake. Bull. Seis. Soc. Am. 91 (5), 995–1012.

Yue, L.F., Suppe, J., Hung, J., 2005. Structural geology of a classic thrust belt earthquake: the 1999 Chi-Chi earthquake Taiwan (Mw=7.6). J. Struct. Geol. 27, 2058–2083.

Zoback, M., Moos, D., Mastin, L., 1985. Well bore breakouts and in situ stress. J. Geophy. Res. 90, 5523–5530.

Zoback, M., Zoback, M.L., Mount, V.S., Suppe, J., Eaton, J.P., Healy, J.H., Oppenheimer, D., Reasenberg, P., Jones, L., Raleigh, C.B., Wong, I.G., Scotti, O., Wentworth, C., 1987. New Evidence on the state of stress of the San Andreas Fault system. Science 238, 1105–1111.

Zoback, M., Barton, C., Brudy, M., Castillo, D., Finkbeiner, T., Grollimund, B., Moos, D., Peska, P., Ward, C., Wiprut, D., 2003. Determination of stress orientation and magnitude in deep wells. Int. J. Rock Mech. Min. Sci., 40, 1049–1076.